

Optimization of the giant magneto-impedance effect in $Fe_{20}Ni_{80}$/Cu composite wires by Joule heating annealing

Xiaofeng Pu(濮晓凤), Chaobo Liu(刘超波), Zhoulu Yu(俞周路), Guozhi Chai(柴国志), Junchen Gao(高骏琛), Linchuan Wang(王琳川), Yongang Liu(刘永刚), and Daqiang Gao(高大强)

Citation: Chin. Phys. B, 2026, 35 (**1**): 017504. DOI: 10.1088/1674-1056/adfebd
http://cpb.iphy.ac.cn; http://iopscience.iop.org/cpb

What follows is a list of articles you may be interested in

Model of output characteristics of giant magnetoresistance (GMR) multilayer sensor

Jiao-Feng Zhang(张教凤), Zheng-Hong Qian(钱正洪), Hua-Chen Zhu(朱华辰), Ru Bai(白茹), Jian-Guo Zhu(朱建国)

Chin. Phys. B, 2019, 28 (**8**): 087501. DOI: 10.1088/1674-1056/28/8/087501

Synthesis and electrochemical properties of three-dimensional graphene/polyaniline composites for supercapacitor electrode materials

Zhao Wen (赵文), He Da-Wei (何大伟), Wang Yong-Sheng (王永生), Du Xiang (杜翔), Xin Hao (忻昊)

Chin. Phys. B, 2015, 24 (**4**): 047204. DOI: 10.1088/1674-1056/24/4/047204

Martensitic transformation & related magnetic effects in Ni-Mn-based ferro magnetic shape memory alloys

Wang Dun-Hui (王敦辉), Han Zhi-Da (韩志达), Xuan Hai-Cheng (轩海成), Ma Sheng-Can (马胜灿), Chen Shui-Yuan (陈水源), Zhang Cheng-Liang (张成亮), Du You-Wei (都有为)

Chin. Phys. B, 2013, 22 (**7**): 077506. DOI: 10.1088/1674-1056/22/7/077506

Mn-based antiperovskite functional materials: Review of research

Tong Peng (童鹏), Wang Bo-Sen (王铂森), Sun Yu-Ping (孙玉平)

Chin. Phys. B, 2013, 22 (**6**): 067501. DOI: 10.1088/1674-1056/22/6/067501

Highly sensitive giant magnetoimpedance in a solenoid containing FeCo-based ribbon

Fang Yun-Zhang(方允樟), Xu Qi-Ming(许启明), Zheng Jin-Ju(郑金菊), Wu Feng-Min(吴锋民), Ye Hui-Qun(叶慧群), Si Jian-Xiao(斯剑霄), Zheng Jian-Long(郑建龙), Fan Xiao-Zhen(范晓珍), and Yang Xiao-Hong(杨晓红)

Chin. Phys. B, 2012, 21 (**3**): 037501. DOI: 10.1088/1674-1056/21/3/037501

Optimization of the giant magneto-impedance effect in $Fe_{20}Ni_{80}$/Cu composite wires by Joule heating annealing

Xiaofeng Pu(濮晓凤)[1], Chaobo Liu(刘超波)[2], Zhoulu Yu(俞周路)[1], Guozhi Chai(柴国志)[1], Junchen Gao(高骏琛)[1], Linchuan Wang(王琳川)[1], Yonggang Liu(刘永刚)[3], and Daqiang Gao(高大强)[1,†]

[1] *College of Physical Science and Technology, Key Laboratory of Magnetism and Magnetic Materials, Ministry of Education, Lanzhou University, Lanzhou* 734200, *China*

[2] *Beijing Institute of Spacecraft Environment Engineering, Beijing* 100094, *China*

[3] *College of Physics and Electronic Engineering, Taishan University, Taian* 271000, *China*

(Received 3 July 2025; revised manuscript received 22 August 2025; accepted manuscript online 25 August 2025)

Giant magnetoimpedance (GMI) sensors are increasingly employed in modern magnetic sensing technologies. However, improving the GMI performance of magnetic cores remains challenging due to intrinsic limitations in material properties and structural stability. In this work, we explore the use of Joule heating to enhance the GMI response of $Fe_{20}Ni_{80}$/Cu composite wires. By applying a current of 1.8 A for 10 min, notable improvements in magnetic domain uniformity and a reduction in domain spacing are observed. Under these conditions, GMI ratios reach 1870% in the non-diagonal mode and 1147% in the diagonal mode, respectively, highlighting their potential for applications in high-precision weak magnetic field sensing.

Keywords: giant magneto-impedance, composite wires, Joule heating annealing, circumferential hysteresis loops

PACS: 75.47.De, 72.80.Tm, 75.60.Nt, 75.60.–d

DOI: 10.1088/1674-1056/adfebd **CSTR:** 32038.14.CPB.adfebd

1. Introduction

With the advent of novel magneto-sensitive materials, the giant magneto-impedance effect (GMI) has garnered widespread attention for applications in magnetic sensors, weak magnetic field detection, and high-frequency components.[1–4] Permalloy, due to its excellent soft magnetic properties such as high magnetic permeability, low coercivity, and a low magnetostrictive coefficient, has been widely used in various applications. In particular, for FeNi/Cu composite structural wires, the magnetic layer exhibits a circumferential domain structure, while the non-magnetic core region helps reduce eddy current losses, thereby improving the GMI response.[5–7]

The GMI effect is typically measured in two configurations: diagonal and non-diagonal modes (Fig. 1(a)). In the diagonal mode, the magnetic core functions simultaneously as the input for the AC excitation and the output for the impedance variation. In contrast, the non-diagonal mode employs the magnetic core as the AC signal input, while the pick-up coil wound around the core serves as the output terminal for the induced impedance signal. By utilizing the mutual inductance between the core and the coil, the non-diagonal mode achieves signal amplification and a significantly enhanced impedance response. This configuration is particularly advantageous for magnetic field sensing applications requiring a broad dynamic range and high sensitivity, and has therefore attracted considerable attention in GMI-related composite material research.[8] Interestingly, the non-diagonal mode is structurally consistent with the probe design commonly employed in contemporary GMI sensor architectures.[9–11] Its magnetic field response arises from both permeability variations and core–coil mutual inductance coupling, thereby enhancing the GMI effect. For instance, Man *et al.*[12] prepared FeCo-based amorphous bands with a GMI ratio of 1936.2% in the non-diagonal mode. Wang *et al.*[13] investigated the magnetoimpedance characteristics of Fe-based nanocrystalline bands, which exhibited a GMI ratio of 1200% in the non-diagonal mode.

While the non-diagonal GMI effect has been widely studied, its response in permalloy composite wires, particularly in relation to microstructural evolution under Joule heating annealing (JHA), has yet to be fully elucidated. Notably, JHA not only reduces internal stress in the magnetic core but also induces circumferential magnetic anisotropy and optimizes the domain structure. Optimized JHA parameters exhibit significant noise suppression capabilities through microstructural refinement.[14] Notably, the $Fe_{20}Ni_{80}$ layer in the core–layer structure usually undergoes significant changes in grain structure, magnetic domain dynamics, and magnetic permeability under JHA, leading to variations in the non-diagonal GMI response.[15] Therefore, systematically studying the effects of

†Corresponding author. E-mail: gaodq@lzu.edu.cn

© 2026 Chinese Physical Society and IOP Publishing Ltd. All rights, including for text and data mining, AI training, and similar technologies, are reserved.

JHA on microstructural evolution and non-diagonal GMI behavior is the focus of the present work.

This study aims to treat $Fe_{20}Ni_{80}$/Cu composite wires under various JHA conditions and systematically investigate their coercivity, magnetic domain structure, and circumferential hysteresis loops. Through a comprehensive analysis, we correlate the circumferential dynamic hysteresis loops with domain characteristics and the GMI response, thereby elucidating the mechanisms by which different JHA conditions affect GMI performance. These findings provide an experimental foundation for the design and development of high-performance magnetic sensors and functional magnetic devices.

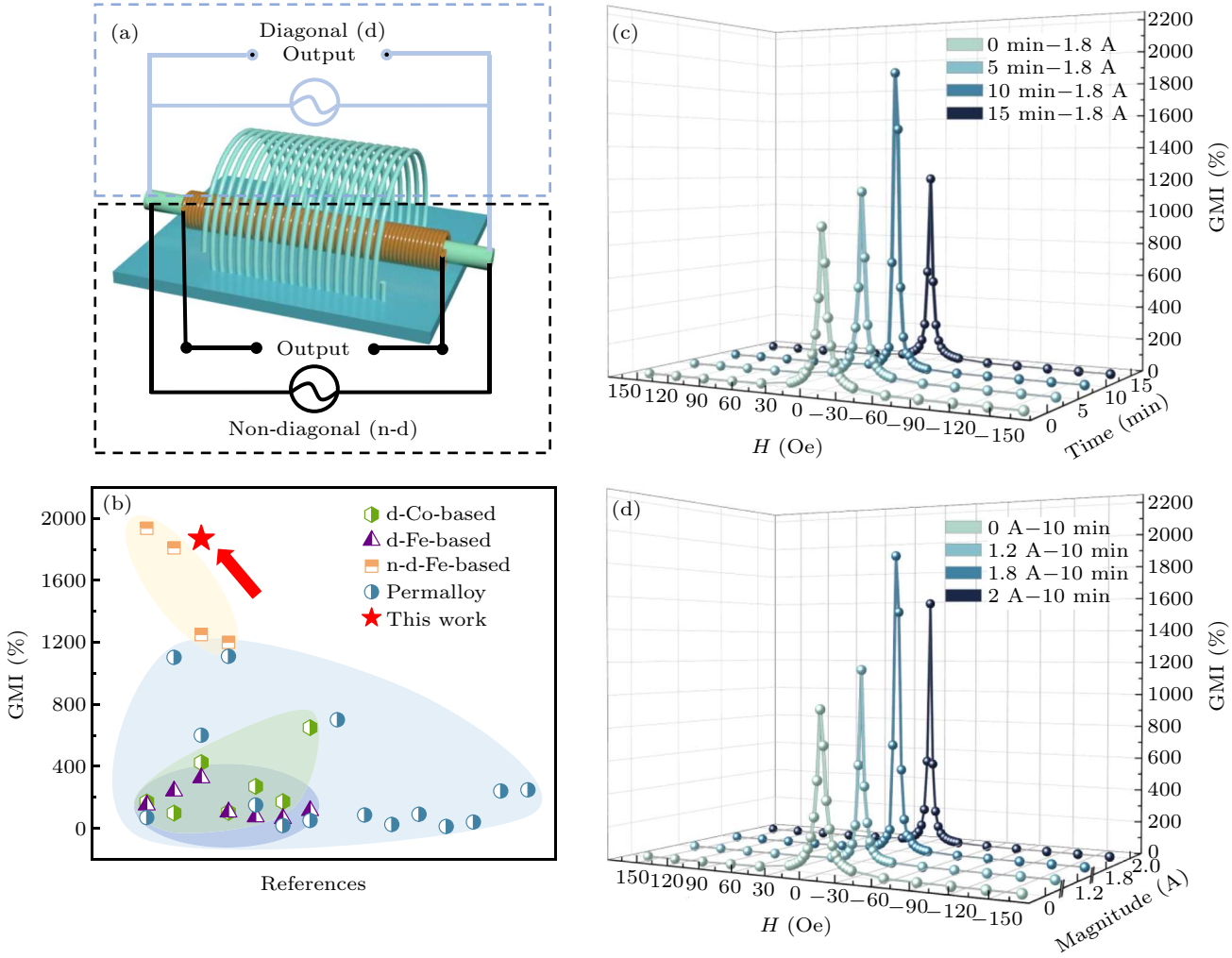


Fig. 1. (a) Diagonal mode (blue circuit) and non-diagonal mode (black circuit) test schematics; (b) comparison of GMI ratios for different materials reported in the literature; (c) GMI ratio under different treatment times at 1.8 A; (d) GMI ratio under different current magnitudes for 10 min, where the GMI value of the 1.8 A–10 min sample reaches 1870%.

2. Methods

2.1. Sample preparation

In this experiment, copper wires with a diameter of 100 μm were used as the substrate. A permalloy ($Fe_{20}Ni_{80}$) coating was deposited on the surface of the copper wire by electrochemical deposition.[16] The electrolyte composition included $NiSO_4$-$7H_2O$ (0.1 mol/L), $FeSO_4$-$7H_2O$ (0.01 mol/L), H_3BO_3 (0.3 mol/L), saccharin (2 g/L), ascorbic acid (5 g/L), and glycine (1 g/L). The deposition conditions were as follows: a current density of 2 A/dm^2, a water bath temperature of 55 °C, a pH value of 2.6, and a deposition time of 4500 s. The resulting permalloy ($Fe_{20}Ni_{80}$) coating had a uniform thickness of approximately 12 μm with good adhesion.

2.2. Magnetic tuning process

To optimize the magnetic properties of the material, the samples were subjected to direct current (DC) treatment under different conditions. The applied currents were 1.2 A, 1.8 A, and 2.0 A, with durations of 5 min, 10 min, and 15 min, respectively. The samples were then allowed to cool naturally to room temperature.

2.3. Characterization and testing methods

Magnetic force microscopy (MFM, Bruker Dimension Icon) imaging was used to investigate the magnetic domain

structures and domain wall characteristics under different treatment conditions. A *BH*-loop analyzer was employed to measure the coercivity (H_c) of the samples, evaluating the impact of JHA on the magnetic properties. Changes in magnetic permeability were calculated by fitting the initial magnetization curves obtained from circumferential hysteresis loops. The GMI effect was tested in the non-diagonal mode using an impedance analyzer (Keysight E4990A) over a frequency range of 0–8 MHz. A sinusoidal AC signal with a frequency of 200 kHz, an amplitude of 3.8 V_{pp}, and a bias of 2.0 V (which may vary depending on the excitation conditions of the sample) was applied using a Keysight 33600A pulse function arbitrary waveform generator as the signal source. The GMI ratio was measured over a frequency range of 0–8 MHz, with the peak maximum concentrated at approximately 400 kHz in the non-diagonal mode and at approximately 40 kHz in the diagonal mode.

3. Experimental results and discussion

The GMI effect of $Fe_{20}Ni_{80}$/Cu composite wires under different JHA conditions was measured in the non-diagonal mode. The GMI response can be expressed by the impedance change formula

$$\frac{\Delta Z}{Z} = \frac{|Z(H) - Z(H_{max})|}{Z(H_{max})} \times 100\%. \quad (1)$$

Here, $Z(H)$ represents the impedance at a given magnetic field, $Z(H_{max})$ represents the impedance under the maximum applied magnetic field, and $\Delta Z/Z$ denotes the maximum impedance change ratio. A higher GMI ratio indicates greater impedance sensitivity to magnetic field changes, which correlates with the dynamic motion of domain walls under the applied field. Figures 1(c) and 1(d) show that the GMI value exhibits a nonlinear dependence on the treatment current and time, which is closely related to domain structure rearrangement and changes in pinning barriers. It can be seen that the GMI ratio gradually increases and then decreases with increasing treatment time and current, reaching a maximum value of 1870% at 1.8 A–10 min. The GMI ratios for other treatment conditions of $Fe_{20}Ni_{80}$/Cu are shown in Fig. S1. Importantly, the GMI properties obtained in this study are superior to those of Co-based and Fe-based amorphous materials in diagonal mode (d-Co/Fe-based), previously reported permalloy composite structural wires, and Fe-based amorphous materials in non-diagonal mode (n-Fe-based), as indicated by the red five-pointed star in Fig. 1(b).[17–41] The composite structure is therefore considered one of the most promising high-performance GMI materials for industrial applications, owing to the significantly higher conductivity of the inner substrate compared with the plating layer, which effectively reduces eddy current losses. Furthermore, its simple fabrication process facilitates mass production at lower cost, further enhancing its industrial applicability.

The GMI ratio measured in the diagonal mode is shown in Fig. S2. Similarly, the GMI ratio of 1147% achieved under the optimal JHA conditions is also competitive compared with previously reported diagonal-mode data shown in Fig. 1(b) (this plot compares only reported GMI ratios on the Y-axis, while the X-axis represents different studies without quantitative meaning). Importantly, under identical conditions, the GMI ratio in the non-diagonal mode is approximately 1.6 times that in the diagonal mode. This enhancement arises from the mutual inductance between the magnetic core and the pick-up coil. The magnetic signal variations in the core collected by the copper coil are amplified in the non-diagonal mode, enabling more sensitive signal output through a conventional probe structure, particularly for weak magnetic field detection. To further clarify these advantages from a material physics perspective, $Fe_{20}Ni_{80}$ exhibits near-zero magnetostriction ($\lambda \approx 0$),[42–44] which significantly suppresses magnetic property fluctuations caused by residual stresses compared with stress-sensitive Co-based amorphous alloys. Its relatively high conductivity (1.5×10^6 S/m)[45] enables a shallower skin depth and enhanced induced electric fields at equivalent frequencies, thereby boosting the magneto-impedance response while reducing power consumption. The composite structure is therefore regarded as a promising candidate for high-performance GMI applications, because the excitation current primarily flows through the copper core owing to its much higher conductivity than that of the plating layer. This efficient current distribution enhances the utilization of the excitation signal, in contrast to Co-based amorphous alloys, in which the current is mainly confined to the surface, leading to insufficient excitation of the internal region.

To investigate the underlying mechanisms behind these remarkable changes, a series of experiments were conducted. As shown in Figs. 2(a) and 2(b), analysis of the hysteresis loops shows that H_c initially decreases and then increases with changes in the treatment current conditions. The as-prepared sample exhibits higher internal stresses, resulting in a stronger pinning effect on domain walls and thus a higher coercivity (1.2 Oe). Under the optimal conditions (1.8 A for 10 min), the coercivity reaches its minimum value (0.6 Oe), indicating that internal stresses are effectively released, domain wall motion is least hindered, and the magnetization process is easiest.[46] Under excessive treatment conditions, grain coarsening and the reintroduction of internal stresses lead to an increase in coercivity.[47]

To further validate the internal stress release behavior during heat treatment, we compared the XRD diffraction peak position variations of samples in different states, as shown in Fig. S3. The untreated sample exhibits a leftward shift

of approximately 0.1° in the diffraction peaks corresponding to the (111), (200), and (220) crystal planes compared with the treated samples, indicating relatively larger lattice spacing and suggesting the presence of a certain degree of tensile stress.[48–50] After annealing treatment at 1.8 A–10 min, the peak positions shift rightward overall, approaching the standard 2θ positions of stress-free crystals. This behavior demonstrates that lattice distortion tends to recover and residual stresses are effectively released. The consistent diffraction peak shifts across multiple crystal planes provide clear qualitative evidence for the evolution of internal stresses.

Further analysis of domain imaging data provides deeper insights into the mechanism by which domain structure optimization affects the GMI effect. The images show the domain structures under different treatment conditions (Figs. 3(a)–3(f)), as well as the corresponding magnetic signal amplitude distribution curves as a function of position under various conditions (Figs. 3(g) and 3(h)). By optimizing the treatment conditions, the stability of domain wall motion and the magnetic response characteristics of the samples can be effectively enhanced. For the as-prepared sample (0 min–0 A), the domain structure is disordered, exhibiting chaotic stripe orientations. This uneven distribution results from high internal stress and microscopic defects (such as grain boundaries and pores) introduced during the electrochemical deposition process, leading to a strong pinning effect on domain walls and hindering their free movement.[51] Under treatment conditions of 1.8 A for 5 min and 10 min, the domain structure gradually adopts a regular stripe-like distribution, indicating that JHA effectively releases internal stress and reduces the pinning barrier.[52,53]

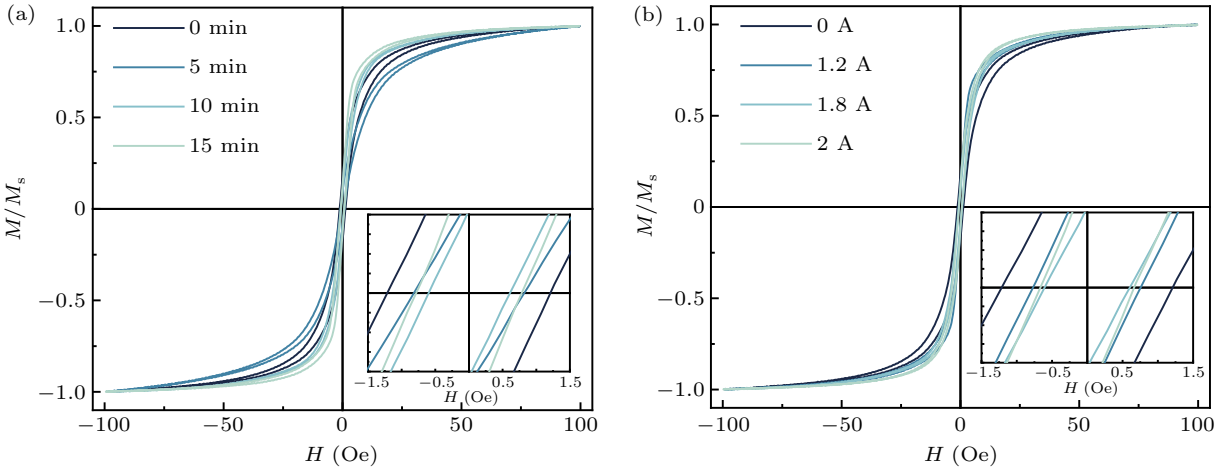


Fig. 2. (a) Effect of different treatment times (at 1.8 A) on coercivity; (b) effect of different current magnitudes (at 10 min) on coercivity, where the 1.8 A–10 min sample exhibits the smallest coercivity.

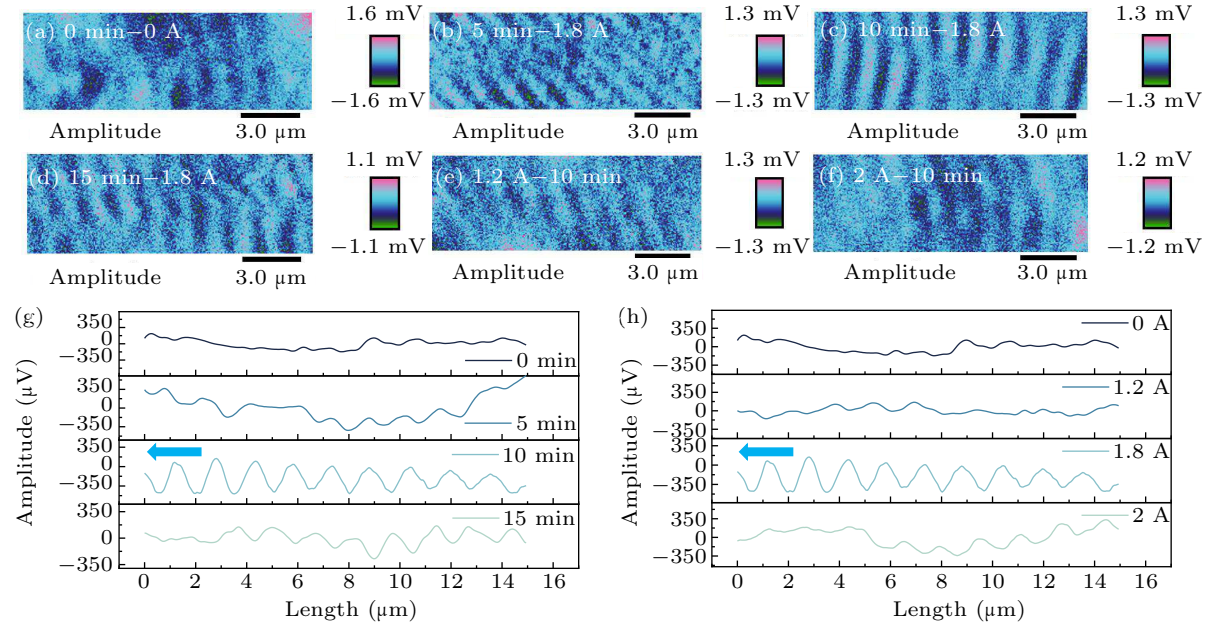


Fig. 3. Variation of domain structure and domain spacing. (a)–(d) Magnetic domain structures under different treatment times; (e)–(f) magnetic domain structures under different treatment current magnitudes; (g)–(h) distribution curves of magnetic signal amplitude as a function of position under different conditions, where the domain structure of the 1.8 A–10 min sample is sharper and the domain spacing is smaller (the blue arrows indicate the direction of decreasing domain spacing).

Under the optimal JHA conditions, the domain structure tends to become more ordered, and the continuity of domain walls and the uniformity of domain sizes are significantly improved. This indicates that internal stress has been effectively released, allowing domain wall motion to become freer, thereby enhancing permeability sensitivity. The optimal balance between stress optimization and avoidance of excessive JHA has been achieved. According to equation in Ref. [54], $\Delta E_{\text{pin}} = \frac{1}{2}ku^2$, k is the elastic coefficient associated with internal stress, and u represents the displacement of the domain wall from its equilibrium position. A comparison between Figs. 3(e) and 3(f) shows that moderate current intensity and treatment time (1.8 A–10 min) significantly reduce k and u, making the domain walls easier to move. Treatment at a lower current intensity (1.2 A) further promotes a regular distribution of domain walls, whereas higher currents (2 A) cause partial domain distortion due to excessive heating.

Figures 3(g) and 3(h) show the distribution of signal amplitude as a function of length for samples treated under different JHA conditions. As shown in the figures, the peak positions of the signal gradually shift, reflecting the dynamic evolution of the domain structure. As the treatment time increases, the waveform becomes more regular, and the domain spacing d becomes homogenized and decreases in the direction indicated by the blue arrow. To quantify this trend, the domain spacing distributions were collated, as shown in Tables S1 and S2. Analysis of the data shows that the domain spacing is inversely proportional to the GMI ratio. For the 1.8 A–10 min sample, the regularity of the signal waveform reaches its maximum, with the domain spacing becoming nearly uniform and minimized, indicating a significant reduction in the domain wall pinning effect. Since the magnetic permeability (μ) is inversely proportional to the domain spacing (d), the optimized JHA conditions lead to a maximum permeability by minimizing d. This is one of the key reasons for the most significant GMI effect observed in this sample.

Fourier transform analysis is used to examine the periodicity of the domain structure in Figs. 3(g) and 3(h). As shown in Fig. 4, short-duration annealing at low current results in a disordered distribution of magnetic domain spacing. The primary peak in the Fourier spectrum is weak, and the GMI ratio is low, indicating limited domain wall motion and minimal changes in permeability. At 1.8 A–10 min, the magnetic domain structure becomes highly uniform, and the primary peak in the Fourier spectrum is sharp and well defined. Domain wall motion becomes synchronized, and permeability variations are more uniform. As a result, the magneto-impedance effect is optimized, leading to the highest GMI ratio. A double-peak feature appears in the Fourier spectrum, which may be caused by resonant behavior of domain walls, further enhancing permeability. When the current increases to 2 A or the annealing time extends to 15 min, the periodicity of the magnetic domain structure deteriorates, and higher-order harmonic components appear in the Fourier spectrum. This behavior suggests stronger disturbances in domain wall motion. Excessive oscillations destabilize the magnetic material and reduce the GMI ratio.

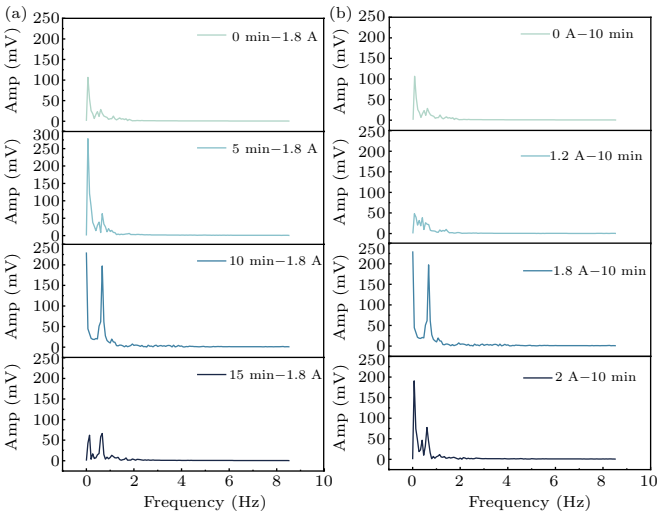


Fig. 4. Analysis of the structural periodicity of magnetic domains using Fourier analysis. (a) different treatment times at 1.8 A; (b) different current magnitudes for 10 min, where the 1.8 A–10 min sample exhibits the most pronounced primary spectral peak with a relatively single distribution, indicating the most uniform magnetic domain spacing.

At the same time, the slope (ξ) of the GMI curve can be defined as the magnetic field sensitivity near zero magnetic field, and the calculation method is shown in Fig. S4, with the following formula:

$$\xi(\%/\text{Oe}) = \frac{\text{d}}{\text{d}H_{\text{ex}}}\frac{\Delta Z}{Z}, \tag{2}$$

where ξ represents the derivative of the GMI with respect to the external magnetic field H_{ex}, corresponding to the slope at the half-peak width of the GMI curve and reflecting the accuracy and sensitivity of the component. Figures 1(c) and 1(d) describe the variation trends of the GMI effect under different treatment times, while Figs. 5(c) and 5(d) summarize the sensitivity under each condition. For the unprocessed sample (0 min), the GMI peak value is relatively low (938%), with a low sensitivity ξ (89%/Oe). For the 5 min treated sample, the GMI peak value increases significantly (1349%), and the sensitivity also increases (113%/Oe). After applying 1.8 A for 10 min, the GMI reaches its maximum peak value (1870%), and the sensitivity also reaches its maximum (322%/Oe). The curve becomes more symmetric, and the peak width increases. After 15 min of treatment, the GMI peak slightly decreases (1640%), and the sensitivity also decreases (132%/Oe).

The same trend is observed with varying current intensities. As the current intensity increases, the GMI effect gradually strengthens. For the 1.2 A sample, the GMI peak increases (1156%), and the sensitivity slightly increases (130%/Oe).

Under the 1.8 A treatment condition, the GMI reaches the maximum peak value (1870%), with a sensitivity of 322%/Oe. When the current intensity is further increased to 2 A during treatment, the GMI peak decreases (1580%), and the sensitivity drops to 175%/Oe. In addition, error bars are included, as shown in Tables S3 and S4. Under small magnetic fields, as shown in Fig. S5, the overall trend remains consistent, with the 1.8 A–10 min condition still exhibiting the maximum GMI response. In the low-field range of 20–30 Oe, the GMI curve shows an approximately linear decrease, indicating that the composite structure exhibits a predictable response under weak magnetic fields. Further calculations show that the residual ratio, GMI%(30 Oe)/GMI%(20 Oe), is approximately 0.3–0.5. This stable near-linear behavior is of significant importance for low-field sensitivity calibration and sensor applications.

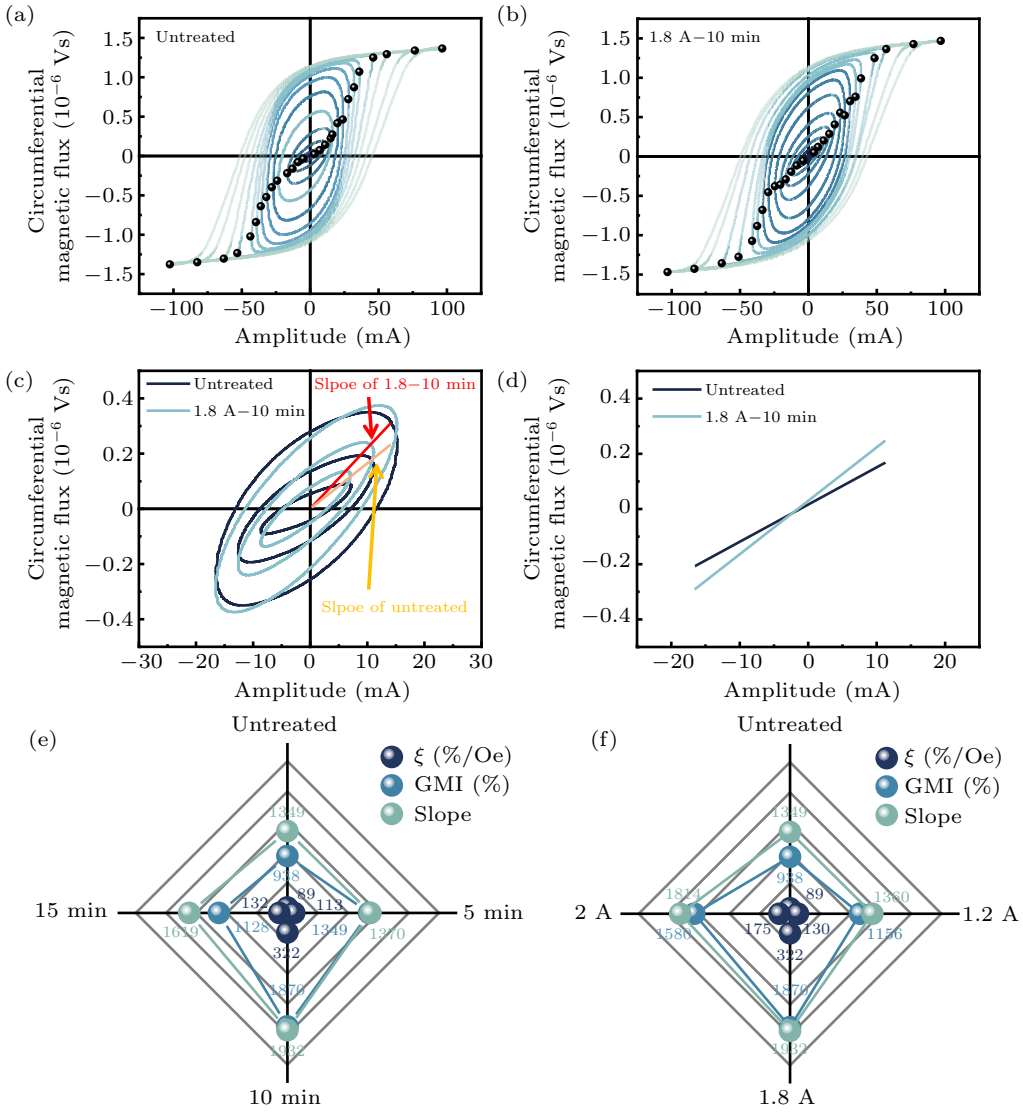


Fig. 5. (a) Circumferential dynamic hysteresis loop and initial magnetization curve of the untreated sample; (b) circumferential dynamic hysteresis loop and initial magnetization curve of the sample under 1.8 A–10 min; (c) schematic diagram of fitting the slope μ_r on the circumferential dynamic hysteresis loop; (d) slope comparison between 1.8 A–10 min and untreated samples, where the slope of 1.8 A–10 min is significantly greater than that of the untreated sample; (e)–(f) comparison of the GMI ratio, sensitivity, and the slope of the initial magnetization curve for different samples. After comparison, the 1.8 A–10 min sample exhibits the best performance.

Furthermore, we separately tested the circumferential dynamic hysteresis loops of the samples under different JHA conditions. The circumferential hysteresis loop describes the relationship between magnetization intensity (M) and the applied magnetic field (H) under the influence of the circumferential magnetic field (i.e., the magnetic field along the material's circumference), which is a critical characteristic for studying filamentous materials.[55,56] As shown in Fig. 6, the signal generator used for loop measurements is the Keysight 81160A, and the oscilloscope is the Siglent SDS2104X Plus. In the constructed test circuit, a resistor R_0 is used to convert the current signal into a voltage signal, which is then captured by the oscilloscope to generate Lissajous figures. The final circumferential AC hysteresis loops were obtained through data processing. To accurately determine the induced voltage, the voltage across the wire's ends is corrected by multiplying the

wire's DC resistance by the current. The induced voltage is obtained by subtracting the calibrated voltage from the measured voltage, and the circumferential magnetic flux density is derived from the following equation:

$$B = \frac{\Phi}{A} = \frac{1}{A}\int V_i \mathrm{d}t = \frac{1}{A}\int (V - IR_0)\,\mathrm{d}t, \tag{3}$$

where A denotes the magnetic flux area within the material, V_i represents the induced voltage, V is the measured voltage, and I and R_0 denote the current flowing through the wire and its DC resistance, respectively.

Consider a cylindrical conductor with radius R and length L. When a current flows through the conductor, J_0 and J_1 are Bessel functions, and the internal magnetic flux (Φ) can be calculated as

$$\begin{aligned}\Phi &= \int_0^R H_\varphi L \mathrm{d}r = -i\cdot\mathrm{const}\cdot\sqrt{\frac{4\pi\mu\sigma i}{\omega}}\,\mathrm{e}^{-\mathrm{i}\omega t} L\int_0^R J_1(kr)\,\mathrm{d}r \\ &= i\cdot\mathrm{const}\cdot\sqrt{\frac{4\pi\mu\sigma i}{\omega}}\,\mathrm{e}^{-\mathrm{i}\omega t} L\frac{1}{k}\left(J_0(kR)-1\right) \\ &= i\frac{c}{\omega}\mathrm{const}\cdot L\left(J_0(kR)-1\right)\mathrm{e}^{-\mathrm{i}\omega t}.\end{aligned} \tag{4}$$

The time derivative of the magnetic flux is then

$$\frac{\partial\Phi}{\partial t} = c\cdot\mathrm{const}\cdot L\left(J_0(kR)-1\right)\mathrm{e}^{-\mathrm{i}\omega t}. \tag{5}$$

The voltage measured across the ends of the wire is approximated as

$$V = E_z L \sim \mathrm{const}\cdot J_0(kR)\,\mathrm{e}^{-\mathrm{i}\omega t}. \tag{6}$$

Under quasi-static conditions, considering only the material's DC resistance, the voltage drop (R_i) across its ends is

$$R_i = IR_0 = \mathrm{const}\cdot\mathrm{e}^{-\mathrm{i}\omega t}. \tag{7}$$

From the above, we have

$$\frac{\partial\Phi}{\partial t} \sim c\left(V - R_i\right) \sim V - R_i \sim V_i. \tag{8}$$

This provides a theoretical basis for the measurement of dynamic hysteresis loops, showing that the loop of a magnetic microwire can be derived by simply measuring the voltage across the wire and the current in the loop.

The raw test data are shown in Figs. 5(a), 5(b), S6 and S7, and its key characteristics include the circumferential initial magnetic permeability μ_r, defined as $\mu_r = \frac{\partial B}{\partial H}\Big|_{H\to 0}$ (extracted by linear fitting of the initial slope of the B–H curve near $H \to 0$). The initial magnetic permeability of the circumferential dynamic hysteresis loop was fitted, as shown by the black dotted data in Figs. 5(a) and 5(b). As shown in Fig. 5(c), the slope fitting diagram is given for the central magnified portion of Figs. 5(a) and 5(b), and the difference of sample loops before and after treatment is compared in Fig. 5(d), showing that the slope of 1.8 A–10 min is significantly higher than that of the untreated sample, indicating a substantial increase in permeability. Additional fitted slope data are shown in Fig. S8, with the fitted slopes tabulated separately and error bars added in Tables S5 and S6. We compiled the slope values under various JHA conditions, summarized in the green data in Figs. 5(e) and 5(f). It was found that changes in the slope generally follow the same trend as the GMI effect ratio. Specifically, the maximum slope of the hysteresis return line was obtained under the 1.8 A–10 min treatment, which is consistent with the magnetic domain behavior shown in Fig. 3, where the sample exhibits the smallest domain spacing and the most regular periodicity. Both features indicate the conditions for achieving the highest GMI effect.

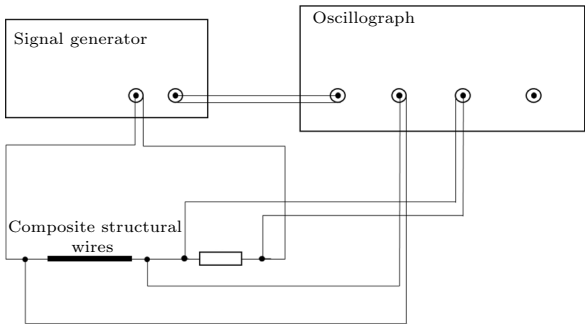


Fig. 6. Schematic diagram of the experimental setup for dynamic hysteresis loop measurement.

Without treated current, the sample exhibits significant internal stress in the magnetic domain structure, leading to strong domain wall pinning effects and lower circumferential magnetic permeability μ_r. As a result, the change in μ_r is minimal, leading to a low GMI peak. As the annealing time and current increase, the circumferential hysteresis loops become progressively steeper (see Figs. S5 and S6)) and the coercivity decreases significantly, while the slope value increases (see Tables S7 and S8). This indicates that the effective loop-wise magnetic anisotropy of the material increases, and the magnetization process occurs more easily. Correspondingly, the magnetic domain images and statistics (see Tables S1 and S2) show a more homogeneous width and reduced spacing of the magnetic domains, indicating a more refined and ordered magnetic structure. This optimization of the magnetic structure through annealing-induced stress release and atomic structure rearrangement contributes to the enhancement of loop permeability and the freedom of motion of the magnetic domain walls, which ultimately manifests in higher GMI effectiveness and sensitivity. All data of regular changes are shown in Tables S7 and S8. At the same time, the increase in hysteresis loop slope also indicates that the material exhibits higher loop magnetization, which is an important characterization of improved performance.

4. Conclusion

Based on these results, the magnetic properties of $Fe_{20}Ni_{80}$/Cu composite wires under different JHA conditions are systematically analyzed, and the relationship between coercivity, domain structure, circumferential permeability, and GMI effect is revealed. The experimental results show that under the optimal JHA condition (1.8 A, 10 min), the composite structure conductor exhibits the lowest coercivity, excellent soft magnetic performance, the highest circumferential permeability slope, and significantly enhanced GMI effect and sensitivity, reaching 1870% and 322%/Oe, respectively. The improvement of magnetic properties is attributed to the JHA process, which effectively releases internal stress, promotes reduction of domain spacing, and reduces the domain wall pinning effect. This research demonstrates high-sensitivity and high-GMI performance, with significant application potential in weak magnetic field detection, intelligent sensors, and high-frequency magnetic devices.

Acknowledgments

This project was supported by the State Key Research and Development Program, Special Gravity Wave (Grant No. 2023YFC2206003), the Gansu Provincial Science and Technology Program Funding (Grant No. 24JRRA499), the Natural Science Foundation of Shandong Province (Grant No. ZR2024QB219), and the Lanzhou City Science and Technology Program Project (Grant No. 2025-2-47).

References

[1] Wang Z, Wen T, Su W, Hu C, Chen Y, Hu Z, Wu J, Zhou Z and Liu M 2020 *IEEE Trans. Ind. Electron.* **68** 7577
[2] Gonzalez A, Zhukova V, Corte-León P, Blanco J and Zhukov A 2025 *J. Alloys Compd.* 179450
[3] Barrera G, Celegato F, Vassallo M, Martella D, Coïsson M, Olivetti E S, Martino L, Sözeri H, Manzin A and Tiberto P 2024 *Sensors* **24** 4902
[4] Guo Y B, Wang D, Wang Z M, Ma L and Zhao Z J 2023 *Chin. Phys. B* **32** 070703
[5] Wang R, Li X, Kong X, Guo Y, Ruan J and Zhao Z 2013 *Nano-Micro Lett.* **5** 140
[6] Yuan W, Wang X, Zhao Z, Ruan J, Li X and Yang X 2004 *Sci. Bull.* **49** 1002
[7] Luo F, Luo Z, Hu W, Li G, Li Y, Liu X and Wang J 2019 *J. Magn. Magn. Mater.* **484** 218
[8] Pasynkova A, Lepalovskii V, Svalov A, Volochaev M and Kurlyandskaya G 2022 *Phys. Met. Metallogr.* **123** 715
[9] Traore P S, Asfour A, Yonnet J P and Dolabdjian C 2017 *IEEE Sens. J.* **17** 6175
[10] Traore P S, Asfour A, Yonnet J P and Boudinet C 2018 *Sens. Actuators A Phys.* **271** 290
[11] Pu X, Zhou Q, Chai G and Gao D 2024 *J. Magn. Magn. Mater.* **592** 171822
[12] Man Q, Fang Y, Sun H and Ye F 2008 *Sci. Bull.* **53** 329
[13] Wang Z, Gong F, Yang X, Zeng L, Chen G, Yang J, Qian S and Yang D 2000 *J. Appl. Phys.* **87** 4819
[14] Yan B, Zhu W, Sun Y, Lu Z, Zhuang X and Fang G 2024 *IEEE Sens. J.* **24** 9792
[15] Tandon P and Mishra A C 2022 *J. Mater. Sci.: Mater. Electron.* **33** 18311
[16] Lee S A, Yang J W, Choi S and Jang H W 2021 *Exploration* **1** 20210012
[17] Beato-López J J, Lete N, García-Arribas A and Gómez-Polo C 2022 *Sens. Actuators A Phys.* **340** 113520
[18] Chlenova A A, Moiseev A A, Derevyanko M S, Semirov A V, Lepalovsky V N and Kurlyandskaya G V 2017 *Sensors* **17** 1900
[19] Chobaomsup V, Jantaratana P and Boonyongmaneerat Y 2018 *Mater. Sci. Forum* **928** 235
[20] da Silva G H B, Ribeiro P R T, Vilela G L S, Raktkovisk D R, Abrão J E, Santos E, Azevedo A, Rodrigues A R, Padrón-Hernández E, Rezende S M and Machado F L A 2022 *J. Magn. Magn. Mater.* **560** 169678
[21] Fuks A A, Aksenov O I, Matveev D V and Aronin A S 2025 *J. Magn. Magn. Mater.* **614** 172712
[22] Li X P, Zhao Z J, Chua C, Seet H L and Lu L 2003 *J. Appl. Phys.* **94** 7626
[23] Man Q, Fang Y, Sun H and Ye F 2008 *Sci. Bull.* **53** 329
[24] Sarkar P, Lu C C, Jeng J T, Yuan F T, Lai M H, Chiriac H, Lupu N and Chang C R 2019 *J. Magn. Magn. Mater.* **474** 107
[25] Shi L, Ruan J, Zhang J, Zhao Z, Gao H B and Hartmann U 2009 *Phys. B: Condens. Matter* **404** 3766
[26] Shuai S, Lu S, Xiang Z and Lu W 2022 *J. Magn. Magn. Mater.* **551** 169131
[27] Song Z, Yuan W, Zhao Z, Ruan J, Yang X, Seet H L and Li X P 2006 *IEEE Trans. Magn.* **42** 2799
[28] Tung M T, Dung D V A, Long N D and Le A T 2012 *J. Supercond. Nov. Magn.* **25** 2499
[29] Vasam S and V S 2020 *J. Electrochem. Soc.* **167** 132503
[30] Wang R L, Zhao Z J, Liu L P, Yuan W Z and Yang X L 2005 *J. Magn. Magn. Mater.* **285** 55
[31] Wang Z C, Gong F F, Yang X L, Zeng L, Chen G, Yang J X, Qian S M and Yang D P 2000 *J. Appl. Phys.* **87** 4819
[32] Xie L, Li X, Zou J T, Pan H L, Xie W H and Zhao Z J 2018 *Surf. Coat. Technol.* **334** 158
[33] Zhang J Q, Qin Y J, Fang Z, Fan X Z, Ma Y, Li W Z, Yang H Y, Kuang F L, Zhai Y, Shi Y L, Dang W Q, Ye H Q and Fang Y Z 2022 *Acta Phys. Sin.* **71** 237501
[34] Zhang Q, Mao Q, Ruan J, Wang Q, Yang X and Zhao Z 2008 *J. Magn. Magn. Mater.* **320** 2319
[35] Zhang S L, Chai Y S, Fang D Q, Wang L C, Xing D W and Sun J F 2014 *Rare Met.* **35** 344
[36] Zhou Z, Zhou Y and Cao Y 2008 *J. Magn. Magn. Mater.* **320** e967
[37] Zhukova V, Corte-Leon P, Ipatov M, Blanco J M, Gonzalez-Legarreta L and Zhukov A 2019 *Sensors* **19** 4767
[38] Ripka P, Platil A, Kaspar P, Tipek A, Malatek M and Kraus L 2003 *J. Magn. Magn. Mater.* **254** 633
[39] Zhou S, Hu J and Quan B 2001 *Mater. Sci. Eng. A* **304** 954
[40] Zhang Q, Mao Q, Ruan J, Wang Q, Yang X, Zhao Z, Seet H and Li X 2008 *Surf. Rev. Lett.* **15** 753
[41] Yang G, He X, Fan X, Zhou C, Zhao J, Wang H, Xiao F and Fang Y 2014 *Adv. Condens. Matter Phys.* **3** 1
[42] Butta M and Schutte B P 2019 *IEEE Trans. Magn.* **55** 4002906
[43] Bozorth R 1953 *Rev. Mod. Phys.* **25** 42
[44] Renuka Balakrishna A and James R D 2021 *Appl. Phys. Lett.* **118** 212404
[45] Arnold H and Elmen G 1923 *Bell Syst. Tech. J.* **2** 101
[46] Zhukov A, Talaat A, Churyukanova M, Kaloshkin S, Semenkova V, Ipatov M, Blanco J and Zhukova V 2016 *J. Alloys Compd.* **664** 235
[47] Gonzalez A, Zhukova V, Ipatov M, Corte-Leon P, Blanco J and Zhukov A 2022 *AIP Adv.* **12** 035021
[48] Fewster P F and Andrew N L 1998 *Thin Solid Films* **319** 1
[49] Noyan I, Huang T and York B 1995 *Crit. Rev. Solid State Mater. Sci.* **20** 125
[50] Bushroa A, Rahbari R, Masjuki H and Muhamad M 2012 *Vacuum* **86** 1107
[51] Coisson M, Tiberto P, Vinai F, Tyagi P, Modak S and Kane S 2008 *J. Magn. Magn. Mater.* **320** 510
[52] Jiang S, Eggers T, Thiabgoh O, Xing D, Fei W, Shen H, Liu J, Zhang J, Fang W and Sun J 2017 *Sci. Rep.* **7** 46253
[53] Chen D, Xing D, Qin F, Liu J, Shen H, Peng H, Wang H and Sun J 2014 *J. Appl. Phys.* **116** 053907
[54] Anderson P M, Hirth J P and Lothe J 2017 *Theory of Dislocations* (Cambridge: Cambridge University Press)
[55] Schmidt N and Guldner H 1996 *IEEE Trans. Magn.* **32** 489
[56] Jiang H, Zhang J, Xu Z, Xu Y, Chen K, Li G, Zeng P and Qu T 2020 *IEEE Trans. Magn.* **56** 1